ACS APPLIED MATERIALS & INTERFACES

www.acsami.org

Research Article

Anisotropic Luminophore Emission for Enhanced Light Trapping in Luminescent Solar Concentrator Waveguides

Tom Veeken,* Kyra Orbons, Nelson de Gaay Fortman, Aurelio A. Rossinelli, David J. Norris, A. Femius Koenderink, and Albert Polman

Cite This: https://doi.org/10.1021/acsami.5c21066

Read Online

ACCESS | Metrics & More | Article Recommendations | Supporting Information

ABSTRACT: Control over the concentration of light is of great importance for many optical systems. Light-emitting diodes (LEDs), lasers, and optical amplifiers necessitate control over the emission of light inside and out of the system. Optical sensors, detectors, and photovoltaic systems typically benefit from light trapping. To achieve enhanced light trapping in an optical waveguide, we demonstrate anisotropic luminophore emission in a luminescent solar concentrator (LSC) waveguide geometry. By embedding CdSe-CdZnS nanoplatelet emitters into high-index TiO_2 nanocylinders, we alter their angular emission profile to increase emission into total internal reflection (TIR) angles. The emission direction can be controlled by optimizing Mie-like multipolar resonances in the individual nanocylinders and the interaction with the lattice. Angle-resolved photoluminescence measurements on the fabricated nanocylinder arrays corroborate this understanding. By optimizing the cylinder shape and lattice spacing, we show an increase in emission into TIR angles from 75% (isotropic emission) to 83.5%. This novel approach to the integration of nanoscale photonic structures and emitters paves the way for enhanced emission control in photovoltaic systems, as well as in solid-state lighting and smart displays.

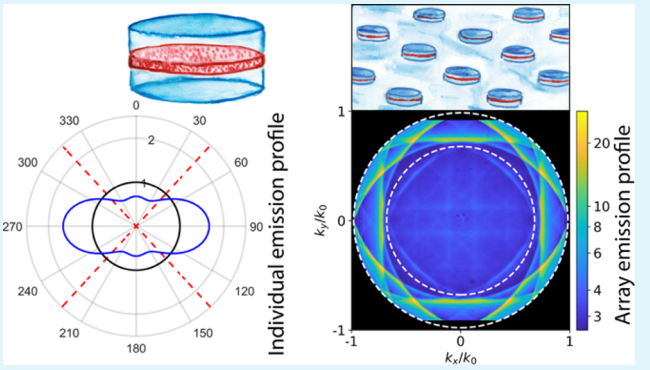

KEYWORDS: *light trapping, optical waveguides, luminescent solar concentrator, photovoltaics, photonics, anisotropy*

INTRODUCTION

Solar photovoltaics (PV) currently makes up about 0.6% of the world's energy production, or 6.2% of electricity production,[1] and keeps growing at a high pace (30% in 2024).[2] To sustain this growth, a large global research effort is well underway to develop further several PV technological families.[3,4] Besides the continued deployment of solar farms, where economies of scale push the installed capacity up by decreasing costs,[5] many other complementary PV technologies have emerged.[6] Building-integrated photovoltaics (BIPV) is a set of such a technologies in which solar power generation is incorporated into the built environment: e.g. in building envelopes,[7,8] roofs,[9] windows,[10−14] greenhouses,[15,16] public spaces,[17] and art.[18] BIPV receives much attention because of their potential to minimize the use of land for PV systems, decrease the overall system and installation costs due to its multifunctional use, and make PV systems more aesthetically appealing.

The photovoltaic luminescent solar concentrator (LSC) is a BIPV device that consists of a dielectric waveguide with embedded luminophores and integrated solar cells along the edges or in a matrix (see Figure 1a).[19] Part of the sunlight transmitted into the waveguide is absorbed by the luminophores, given by their absorption band and particle concentration (optical density, OD). The luminophores subsequently emit photoluminescence (PL) at lower energy, set by the Stokes shift. The photoluminescence quantum yield (PLQY) indicates the efficiency of emission after absorption. A fraction of the PL is trapped in the waveguide by total internal reflection (TIR). The spectral profiles and intensity of the absorption and emission of the luminophores, in combination with the optical pathways in an LSC (Figure 1b), determine the opacity and color of the LSC.[20]

Compared to conventional flat photovoltaic cells, LSCs offer superior mechanical flexibility, lower operating temperatures,[22] resistance to optical shading effects,[23] and use less active photovoltaic material. Geometric concentrating photovoltaic systems have limited acceptance angles and therefore require sun-tracking, whereas LSCs are passive concentrators that absorb both direct and diffuse irradiance.[24,25] Finally, the distinct

Received: October 21, 2025
Revised: June 29, 2026
Accepted: July 6, 2026

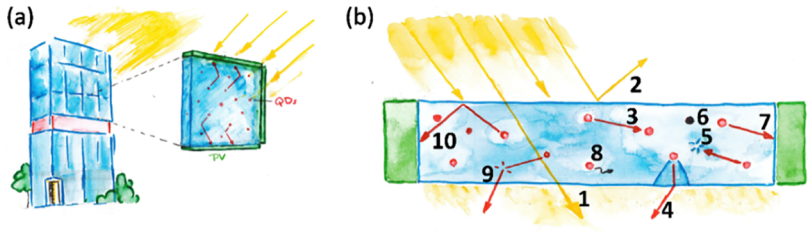

Figure 1. (a) Schematic representation of a luminescent solar concentrator as a building-integrated photovoltaic device. (b) Overview of the optical pathways in an LSC: 1) represents light that is not absorbed by a luminophore, 2) reflection at the surface, 3) reabsorption, 4) escape cone loss, 5) parasitic absorption by the waveguide, 6) long-term luminophore instability, 7) parasitic losses in the solar cell, 8) limited photoluminescence quantum efficiency, 9) internal scattering, and 10) total internal reflection.[21]

absorption spectra of ultra-high (>99%) PLQY luminophores[26] make the LSC a promising candidate for future tandem devices.[27–30]

The key device parameters that must be tuned when designing an LSC[21,31] are the PLQY, OD, and the luminophore absorption and emission spectra. The refractive index sets the critical angle for TIR inside the waveguide, while the Stokes shift imposes the maximum achievable concentration.[32,33] The absorption onset of the PV should be aligned with the luminophore emission spectrum to minimize carrier thermalization in the PV. The geometric gain (GG) of an LSC is the ratio of the waveguide's top surface area to the active PV surface area; higher GG due to increased top surface area increases the average optical path length to the PV cell, thereby amplifying loss pathways.

Despite several decades of LSC research, interplaying loss mechanisms still limit its potential.[21] Novel luminophores, such as highly emissive perovskites and colloidal quantum dots,[34,35] have largely replaced the traditional organic dye molecules that suffered from limited spectral coverage, low PLQY, and small Stokes shifts leading to strong reabsorption losses.[36] Yet, the record power conversion efficiency of 7.1%, for a GG of 2.5 and 1 sun illumination, is still reported for a dye-based LSC.[37] Figure 1b shows the optical pathways in an LSC.[21] The emission of photons through the escape-cone is a major loss channel, accounting for over 25% of all emitted photons. This is a direct consequence of the typical isotropic luminophore emission in the waveguide matrix and the critical angle of a glass/plastic, parallel-plane waveguide in air that sets the single-pass trapping by TIR at 75%.

Much computational and experimental research has aimed to reduce the escape cone losses in LSCs. For instance, by selectively reflecting light at the luminophore emission wavelength with Bragg mirrors placed on the top and bottom surface of the LSC.[38–40] Partially limiting escape cone emission angles with Bragg mirrors has also been proposed for an LSC with an external PV.[41] An alternative approach is to alter the angular emission profile of the luminophore to emit more into TIR angles, for example, by adjusting the luminophore shape,[42,43] orientation,[44] or nanophotonic environment.[45] In a previous work, we systematically evaluated the effect of anisotropic luminophore emission on the power conversion efficiency using a Monte Carlo ray-tracing model. The results imply that strong anisotropic emission into TIR angles in combination with ultra-high PLQY[26] unlocks power conversion efficiencies towards the single-junction detailed-balance limit.[31]

In this work, we present and demonstrate a novel nanophotonic approach to anisotropic luminophore emission to enhance light trapping in an optical waveguide, specifically with the application in LSCs in mind. By directly embedding luminophores into high-index TiO_2 nanocylinder arrays, we increase emission into TIR angles. The shape and size of the cylinder arrays are optimized such that the Stokes-shifted luminophore emission is resonantly directed in-plane. The simulations predict that the escape cone losses at the single resonator level are reduced from 25% to 14.7% in the optimized design. Subsequently, rigorous coupled-wave analysis simulations are performed to find the optimal lattice constant for the array of cylinders, predicting reduced escape cone losses of 16.5%. We fabricated arrays of TiO_2 nanocylinders on top of a glass substrate with integrated highly-emissive CdSe-CdZnS core-shell nanoplatelets, according to the optimized design. Angle-resolved photoluminescence microscopy measurements show strong anisotropic emission, in excellent agreement with the simulated profiles.

NANOPHOTONIC ANGULAR EMISSION CONTROL

Nanophotonic angular emission control of dipole-like emitters[46–48] is a promising route to improve various photovoltaic systems and has thus been studied extensively.[5,49] Unidirectional emission was first demonstrated by placing QDs in the vicinity of plasmonic nanoantennas.[50,51] By employing an array of resonators, the emitter can couple to diffractive lattice modes.[52,53] Directional emission was demonstrated by coupling emitters to all-dielectric nanophotonic resonators.[54] Lasing from semiconductor nanocrystals has also been demonstrated by coupling them to plasmonic[55,56] and dielectric nanoparticle arrays.[57] Previously, we have shown directional emission of semiconductor QDs by soft-stamping them onto silicon nanocylinders that exhibit Mie-like multipolar resonances.[58]

Here, we directly embed colloidal CdSe-CdZnS core-shell nanoplatelets[59] in high-index TiO_2 nanocylinder arrays. The nanoplatelets (NPLs) are identical to those reported in reference:[59] they have a center emission wavelength of 655 nm, a full-width half-maximum (FWHM) linewidth of 19.5 nm, PLQY of 88%, excitonic absorption peak at 590 nm, and Stokes shift of 209 meV. In this system, we avoid enhanced parasitic absorption losses typical of plasmonic or absorbing dielectric systems, control the precise location of the emitters with respect to the TiO_2 resonator, and control the shape of the resonators. The TiO_2 nanocylinders exhibit multipolar Mie-like resonances[60,61] due to the high refractive index ($n \approx 2.3$ at 650 nm wavelength) and low extinction coefficient ($k \leq 0.003$ beyond 400 nm wavelength)—see Figures S1–S3 in the Supporting Information.

We embed the TiO_2 nanocylinders in a silica glass environment (refractive index: $n = 1.475$) and optimize for the shape

https://doi.org/10.1021/acsami.5c21066
ACS Appl. Mater. Interfaces XXXX, XXX, XXX–XXX

with the best response. Following the procedure by Vaskin et al.,[46] we first optimize the emission into TIR angles for a single nanocylinder. To find the optimal size of the individual nanocylinder, we perform finite-difference time-domain (FDTD) simulations (see the Methods section for details). We use a single, monochromatic ($\lambda = 650$ nm) dipole source in the center of the cylinder (Figure 2a) and optimize its height and diameter. As a result, we obtain a maximum of 93.7% emission into TIR angles for a diameter of 450 nm and height of 150 nm. Figure 2b shows the corresponding angular emission profile as calculated by FDTD (blue), averaged over the three orthogonal dipole moments: *x*, *y*, and *z* oriented. The black line shows the reference case of isotropic emission: 75% of the emission is within the TIR angular range, indicated by the red dashed line (42.7° from normal incidence). The optimized emission profile is normalized to the isotropic case, yielding a local density of optical states (LDOS) enhancement of 4.25 at the cylinder center (see the Methods section for details).

To achieve the desired absorption, a large amount of luminophores is necessary. Therefore, we extend our design to that of a TiO_2 nanocylinder with a planar center layer of luminophores (Figure 2c). The optimization now involves the simulation of dipole sources at several radial and axial positions and subsequently a weighted incoherent summation over positions and dipole orientations to emulate a full sampling of all source positions in the layer. The single dipole source optimization proves a good initial indicator because the optimal shape remains similar: a diameter of 500 nm and height of 150 nm, now with a centered luminophore layer of 30 nm in thickness. Figure 2d shows the resulting angular emission profile (blue) for the ensemble of luminophores positions, again averaged over the three dipole moments, yielding 85.3% emission into TIR angles. The corresponding LDOS enhancement is 3.5. The reduced LDOS is attributed to a change in the coupling between the off-center dipoles and the nanocylinder Mie-like modes.

The Stokes shift allows for the decoupling of the luminophore absorption and emission probabilities, which are otherwise coupled through the principle of reciprocity. This decoupling allows for the optimization of the nanocylinder to promote emission into TIR angles without compromising the absorption of incident light. In fact, the optical cross-section of the nanocylinder can be designed to also enhance absorption in the spectral range that the luminophore absorbs. Here, however, we have not considered the luminophore absorption as a figure of merit during the nanocylinder design. With the optimized cylinder design established, we proceed to the fabrication of TiO_2 nanocylinder arrays with embedded luminophores on a glass substrate (Figures 3a and 4a).

NANOCYLINDER ARRAY FABRICATION

We fabricate the designed structures using a top-down approach, similar to that reported by Ha et al.[62] First, a layer

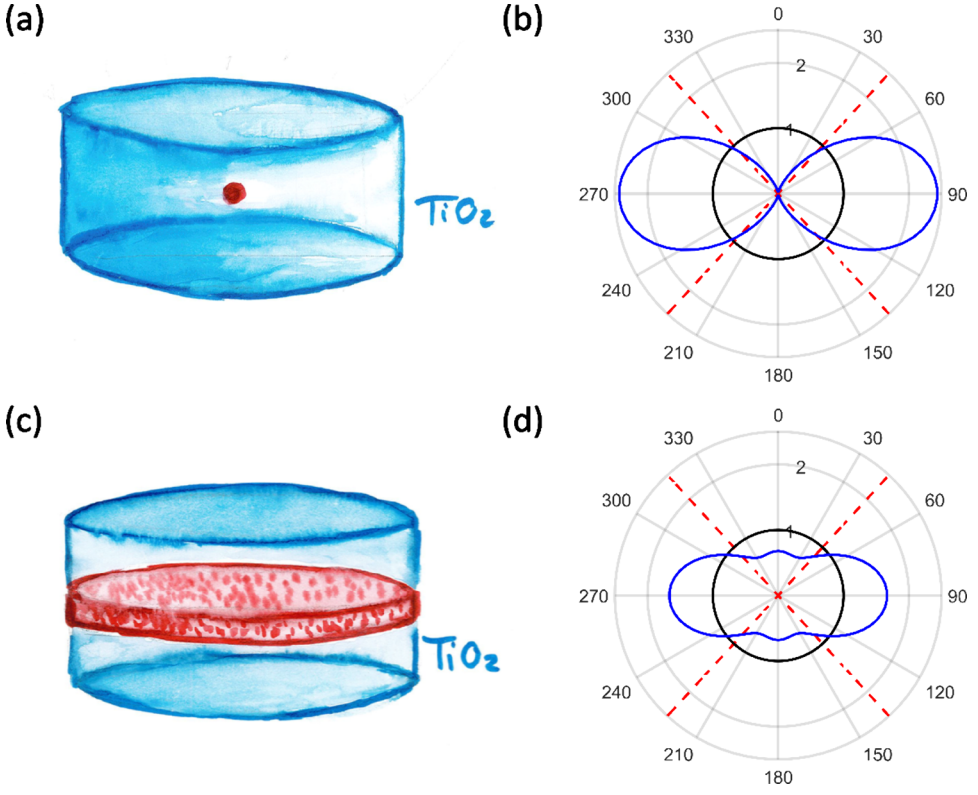

Figure 2. (a) Single dipole-like emitter (red) embedded in the center of a TiO_2 nanocylinder and (b) its corresponding, optimized directional emission profile (blue) at a diameter of 450 nm and height of 150 nm. (c) Layer of emitters (red) embedded in the nanocylinder at center height and (d) its corresponding, optimized directional emission profile (blue) at a diameter of 500 nm and height of 150 nm. Emission profiles are calculated with FDTD, averaged over the three orthogonal dipole moments. The black line shows the reference case of isotropic emission, with 75% emission into TIR angles (red dashed line indicates the critical angle for TIR). The intensity of the optimized emission profiles in blue is normalized by the isotropic case.

https://doi.org/10.1021/acsami.5c21066
ACS Appl. Mater. Interfaces XXXX, XXX, XXX–XXX

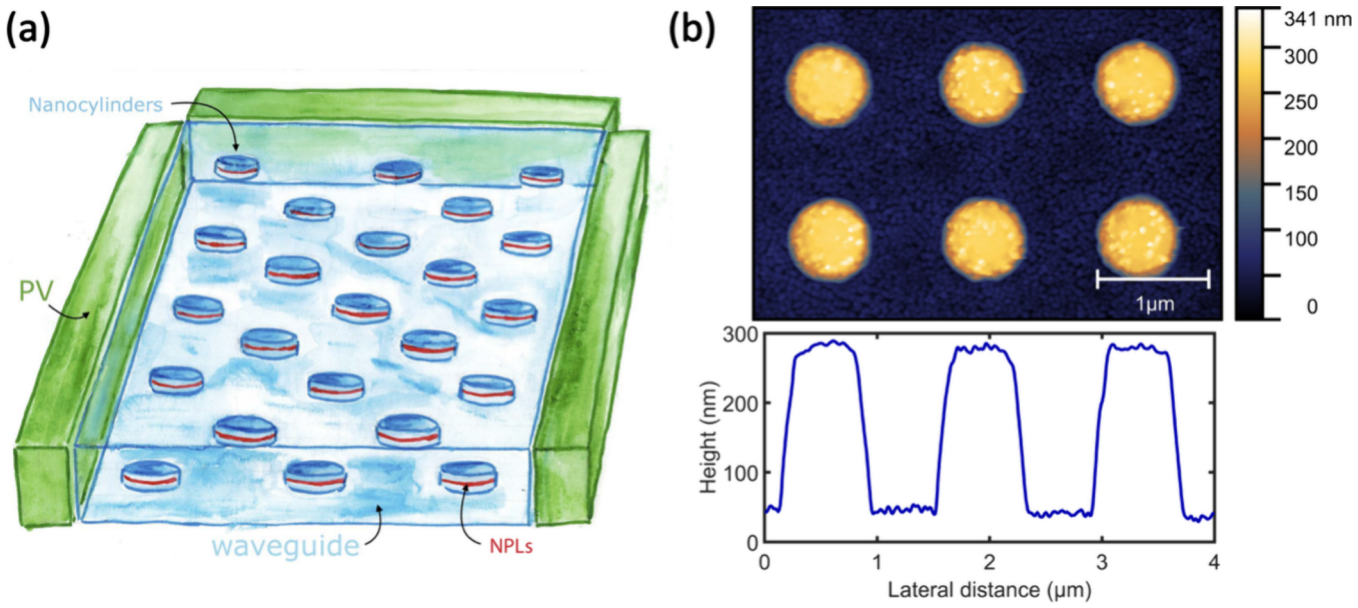

Figure 3. (a) Sketch of a possible implementation of the nanocylinder array inside an LSC. (b) AFM height map of the TiO_2 nanocylinder array with embedded nanoplatelets.

of 60 nm TiO_2 was deposited on a borosilicate glass substrate (500 μm thick) using electron-beam physical vapor deposition (EBPVD). Then a 30 nm layer of CdSe-CdZnS core-shell nanoplatelets (NPLs) was spin-coated, and a final 60 nm TiO_2 layer was evaporated on top. Electron-beam lithography (EBL) and reactive-ion etching were then used to pattern the triple layer on glass into an array of cylinders. A negative tone resist, ma-N 2400, was used as the EBL mask. After EBL exposure and development of the resist, a combination of CHF_3 and O_2 gases was used to etch the structures with RIE (see the Methods section for details). On a single substrate, several fields of 100 × 100 μm cylinder arrays were fabricated by raster scanning of EBL. EBL gives full control over the shapes and sizes of the arrays, which is particularly useful for prototyping but makes the patterning rather slow. Upscaling of this nanostructuring technique is fully feasible with stamping technologies such as soft conformal imprint lithography (SCIL) to obtain large-area RIE masks.[63] Figure 3b shows an atomic force microscopy (AFM) map of the resulting nanocylinder array for target dimensions of 500 nm diameter and 1400 nm pitch. As the initial height of the layer stack was 150 nm, the much deeper AFM profile shows the sample has been etched into the glass substrate. This is not a problem for our experiment because our design considers a homogeneous glass surrounding, and measurements are performed with index-matching fluid covering the cylinder arrays to mimic this glass surrounding. A scanning electron microscopy (SEM) image is also shown in Figure S4 for a nominally identical nanocylinder array that was fabricated on a silicon substrate for reference.

SPATIAL PHOTOLUMINESCENCE MEASUREMENTS

We measured the photoluminescence of the embedded NPLs as a function of position on the nanocylinders array. Figure 4a shows a microscope image taken with a confocal microscope in reflection. In Figure 4b, we plot the photoluminescence

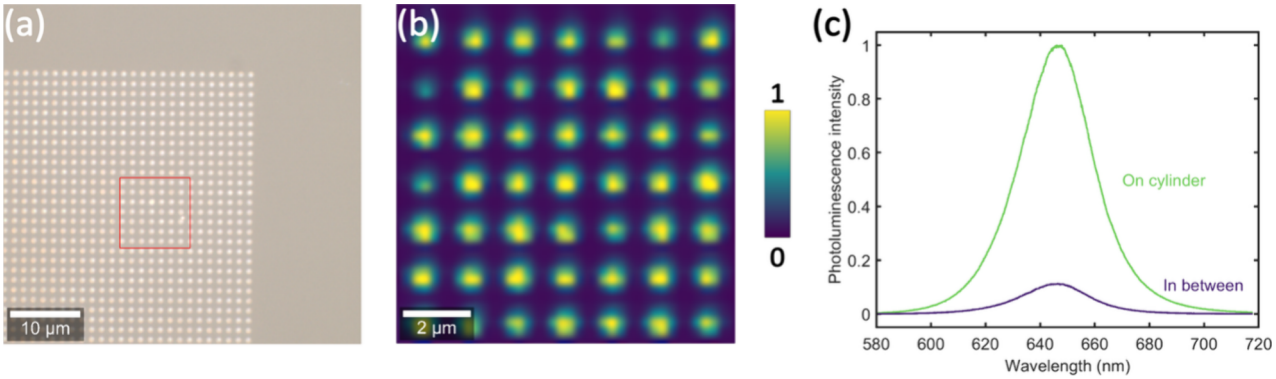

Figure 4. (a) Optical microscopy image of the corner of the TiO_2 nanocylinder array with embedded nanoplatelets. (b) Photoluminescence intensity map of the marked area in panel (a), indicating that emission is confined to the nanocylinders. The color scale depicts the normalized intensity at 650 nm wavelength; pixels have been smoothed with a moving-average filter (original data are shown in Figure S5a). (c) Photoluminescence spectra corresponding to two positions in panel (b): on top of the cylinder and in between four cylinders.

https://doi.org/10.1021/acsami.5c21066
ACS Appl. Mater. Interfaces XXXX, XXX, XXX–XXX

intensity at λ = 650 nm as a function of position, corresponding to the area marked by the red square in Figure 4a. Bright PL is observed when the laser is positioned on top of a cylinder, confirming that the NPLs remain bright emitters after going through all of the fabrication stages (see Figure S5b). Moreover, most cylinders display similar PL intensity, showing that a homogeneous sample was fabricated, and subsequent angle-resolved photoluminescence measurements can be collected from an extended area by exciting multiple cylinders. In Figure 4c, two representative PL spectra are plotted corresponding to the data in Figure 4b: on top of a cylinder (green) and in between four cylinders (purple). We attribute the nonzero intensity for laser excitation positions in between the cylinders to emission from NPLs in the surrounding cylinders. The neighboring NPLs can have been excited through a number of processes, for example due to excitation by the tails of the diffraction-limited laser spot, light scattered by roughness on the etched glass substrate, excitation of Bloch modes of the cylinder array at the laser wavelength, and light funneled towards the cylinders due to their increased optical cross-section at the laser wavelength.[61]

■ ANGLE-RESOLVED PHOTOLUMINESCENCE MEASUREMENTS

Next, we measured the PL as a function of angle with a Fourier microscopy setup (see the Methods section). We measured on a nanocylinder array with 800 nm pitch, illuminating several hundreds of cylinders with the laser excitation spot. Figure 5a shows the obtained angle-resolved PL intensity image as a function of normalized parallel wavevector. The white dashed lines correspond to NA = 1 (critical angle from glass substrate to air) and NA = 1.45 (maximum for the objective), respectively. To analyze these data, we consider the photonic crystal waveguide modes that are described by dispersion relations that relate the locus of allowed wave vectors $(k_x,k_y)_{wg}$ to frequency. In a qualitative picture, where the cylinder-layer can be viewed as an effectively homogeneous slab with just a weak periodic perturbation, the locus of wave vectors is just a circle concentric with $k = 0$, with radius depending inversely on the wavelength, and determined by the guided mode index. Emitters predominantly radiate into these guided modes. The periodic perturbation makes these guided modes accessible to free space light by virtue of grating diffraction, which in k-space expresses as repetition of the dispersion relation of the waveguide at each reciprocal lattice point.[46,64] The data in Figure 5a are well described by concentric circles repeated on a square lattice: we observe vertical and horizontal oval shapes resulting from parts of large, displaced circles.

To model the full angular emission profile of the nanocylinder array, we perform rigorous coupled-wave analysis (RCWA) simulations using the open-source software package S^4 by Liu and Fan[65] (see the Methods section). Similar to the FDTD simulations, we model the structure with experimentally obtained optical constants for TiO_2, but now we place the nanocylinder in periodic boundary conditions. We use reciprocity, according to which far-field emission patterns from sources in the structure can be predicted from the local absorption generated by far-field plane wave incidence at the same wavelength (see the Methods section). To this end, we model the structure in RCWA and include absorption (imaginary part of the refractive index, $k \approx 0.02$) for the nanoplatelet layer inside the TiO_2 cylinders. At the target wavelength of 650 nm, we calculate the absorption in the center layer as a function of azimuthal and polar angle. Figure 5b shows the result for a pitch of 800 nm, normalized and plotted on the same axis as the experimental values in Figure 5a. The experimental and simulated results show clear similarities: a horizontal and vertical shape is present with double bands, and the center shows a cross and diamond shape. However, bands do not appear at quite the same normalized k_x,k_y values, which we attribute to differences between the nanocylinder shape in the simulation and measurement. In general, the high-intensity bands remain within the inner dashed white circle, corresponding to the glass-air escape cone, so enhanced TIR light trapping is not achieved at this pitch.

The measurement and simulation are repeated for nanocylinder arrays with a larger pitch of 1000 nm, 1200 nm, and 1400 nm; the results are shown in Figure 5c–h. Again, we find a good comparison between the high-intensity features in the measured and simulated data. Moreover, the comparison becomes better as the pitch increases. For the largest pitch of 1400 nm, the desired emission profile is obtained for which the high-intensity emission bands are beyond the escape cone. The pitches are chosen between 800 and 1400 nm to ensure the lattice supports waveguide modes at the emission wavelength. Differences in intensity between the simulated and experimental data are partially attributed to the implication of the 'constant current' source used in the simulations (see the Methods section for a detailed discussion). The fact that the features in the experimental data are broader than in the simulated data is attributed to the finite, diffraction-limited excitation spot.

The combination of higher and lower intensity features in Figure 5b,d,f,h are understood as a superposition of photonic crystal waveguide modes that are repeated over the reciprocal lattice. The locations of the maxima are fully determined by the lattice. The intensity distribution of this structure factor is modified by the angular emission profile of the individual cylinder. We observe that the photonic crystal bands in the center have lower intensity than the bands at higher wavevectors, precisely following our design.

Many broader features in the simulated results are combinations of separate modes, as can be seen at some locations in Figure 5b,d. These two modes are waveguide modes for orthogonal polarization, i.e. electric field parallel or perpendicular to the photonic crystal plane, which we will refer to as s and p polarization, respectively. Figure S6 shows the same polarization averaged result as in Figure 5, as well as individual s and p polarization results. Those figures clearly show the two separate modes at similar locations, indicating a slightly different mode index for the orthogonal polarizations.

Extending upon the repeated rings in the k_x,k_y plane, we can obtain a Fourier plane image at several frequencies (wavelengths) of the emitted light. This three-dimensional dataset describes the dispersion of the photonic crystal waveguide modes as the frequency and corresponding wavevector is changed. The rings are extended to cones in 3D, as described in ref 46. Instead of slicing the dataset along a certain wavelength to obtain subsets as shown in Figure 5, we now slice along the $k_y = 0$ plane to depict the dispersion along k_x, revealing the photonic crystal bands as a function of wavelength in Figure 6. The red dashed line indicates a wavelength of 650 nm. In panel (a), we find two bands with

https://doi.org/10.1021/acsami.5c21066
ACS Appl. Mater. Interfaces XXXX, XXX, XXX–XXX

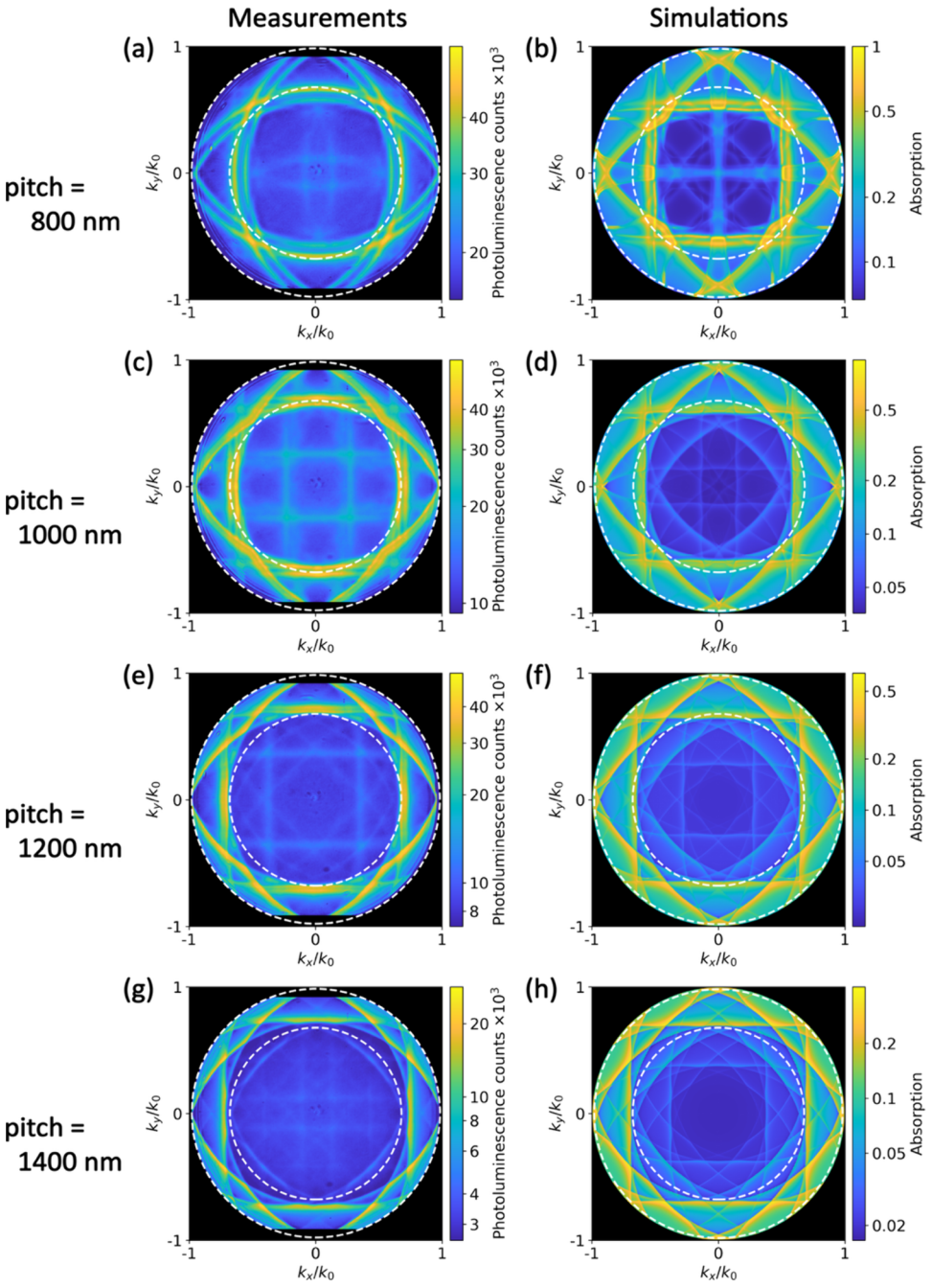

Figure 5. Angle-resolved photoluminescence measured on and simulated for a (a, b) 800 nm, (c, d) 1000 nm, (e, f) 1200 nm, and (g, h) 1400 nm pitch array. The measured results correspond well with the simulated photonic crystal bands. For the largest pitch of 1400 nm, 83.5% of the emitted light is trapped under TIR angles. The white dashed lines correspond to NA = 1 (critical angle from the glass substrate to air) and NA = 1.45 (maximum for the objective). All data are averaged over s and p polarization. Polarization resolved results for the simulated and measured datasets are shown in Figures S6 and S7, respectively, in the Supporting Information.

high intensity that correspond to the high-intensity oval shapes in Figure 5a. Upon increasing the array pitch (Figure 6b–d), the bands move outwards to higher wavevectors for equal wavelength. The slope of the bands remains similar, indicating that the mode indices remain similar upon expanding the array pitch. Given the similar mode index, we explain the movement of the bands to higher wavevectors by the decrease of the reciprocal lattice vector due to the increasing pitch.

Finally, we calculate the emission fraction into TIR angles based on the simulated results in Figure 5. For the 800 nm pitch array, the TIR emission fraction is 68.5%, which is lower than the isotropic reference case of 75%. This suggests that the same design procedure described here could be employed to increase the fraction of light emitted into the escape cone, for example, to increase the outcoupling yield of LEDs or displays. Emission into TIR angles increases steadily from 68.5% (800 nm) to 75.9%, 81%, and 83.5%, for 1000, 1200, and

https://doi.org/10.1021/acsami.5c21066
ACS Appl. Mater. Interfaces XXXX, XXX, XXX–XXX

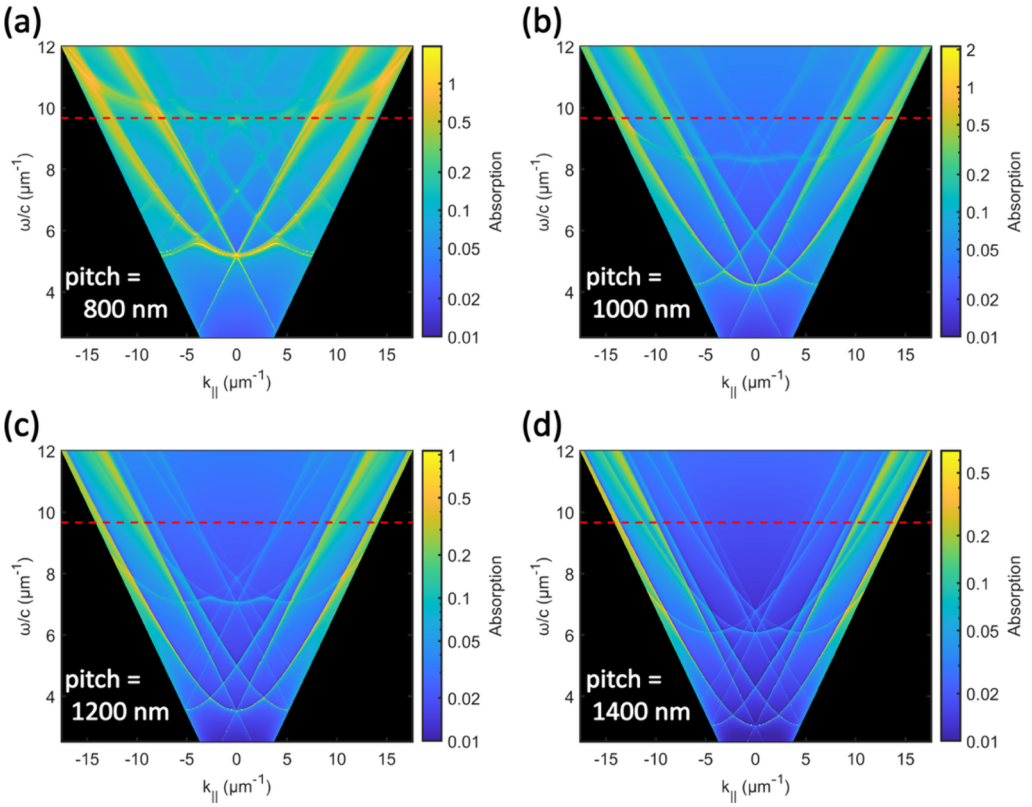

Figure 6. Calculated dispersion diagrams for a (a) 800 nm, (b) 1000 nm, (c) 1200 nm, and (d) 1400 nm pitch array, averaged over s and p polarizations, along the $k_{par} = k_x$ axis and as a function of normalized frequency ($2\pi/\lambda$). The red dashed line indicates the target wavelength of 650 nm, corresponding to a horizontal cut through the plots in Figure 5 at $k_y = 0$. As we already observed in Figure 5 and Figure S6, the photonic crystal bands are displaced outwards with increasing array pitch, which is attributed to a decrease in the reciprocal lattice constant. Polarization resolved results are shown in Figure S8 in the Supporting Information.

1400 nm pitch, respectively. Calculation of the TIR fractions for the measured results is not readily possible because the objective does not collect light emitted beyond the NA, and thus, we do not obtain the emission for grazing angles between 79.4° and 90°. Nevertheless, we can see in Figure 5g,h that the experiment and simulation compare very well, many fine features and relative intensity variations are well reproduced.

■ CONCLUSIONS

In conclusion, we have demonstrated anisotropic luminophore emission as a first step towards the realization of enhanced light trapping in LSC waveguide geometries. By embedding CdSe-CdZnS nanoplatelets into an array of TiO_2 nanocylinders, we alter their angular emission profile to increase emission into the angular range of total internal reflection (TIR). First, we optimized the dimensions of a single nanocylinder with an embedded layer of dipole-like emitters to maximize emission into TIR angles of a typical LSC waveguide. Changing the diameter and height of the cylinder alters the multipolar Mie-like modes it sustains, as well as their strength, and the coupling of the emitters with these localized modes alters their angular emission profile. Subsequently, we designed and fabricated a square lattice of nanocylinders such that emission into lattice modes occurs at angles outside the escape cone. Angle-resolved photoluminescence measurements are in good agreement with simulated emission profiles, corroborating our understanding of the coupling between the emitters and the photonic structures. Finally, we show an increase in light trapping from 75% (isotropic emission) to 83.5%, which could significantly increase LSC power conversion efficiencies. This novel approach to directive emission, by embedding emitters in dielectric nanostructures, can pave the way towards enhanced emission control in photovoltaic systems, as well as many other optical systems such as light-emitting diodes (LEDs), lasers, and optical amplifiers, sensors, and detectors.

■ METHODS

FDTD Simulations

The angular emission profiles for dipoles embedded in a single TiO_2 nanocylinder were calculated using finite-difference time-domain (FDTD) calculations performed in Lumerical FDTD Solutions.[66] Perfectly matched layer (PML) boundary conditions were used in three dimensions. A single, monochromatic electric dipole source was used for each simulation, with a polarization axis along either the *X*-, *Y*-, or *Z*-axis. A "scat_ff" power monitor box was used to collect the electric and magnetic field components surrounding the nanocylinder. Convergence was found at a uniform mesh size of 5 nm, a distance of 250 nm from the structure to each FDTD box boundary, and conformal mesh refinement. To convert the simulated near fields to far field radiation intensities, we used the far field projection function from Lumerical FDTD Solutions. The complex experimental optical constants of TiO_2 as determined by ellipsometry (see the Ellipsometry section) were used.

https://doi.org/10.1021/acsami.5c21066
ACS Appl. Mater. Interfaces XXXX, XXX, XXX–XXX

By keeping a fixed electric dipole amplitude in each simulation ('constant current' or 'constant amplitude' source), the total emitted power is directly proportional to the Purcell factor and the LDOS.[67] Thus, for the two optimized cases in Figure 2, the LDOS enhancement is calculated as the emitted power divided by the emitted power in free space (weighted by incoherent summation over positions and dipole orientations).

RCWA Simulations

To simulate the angle-resolved emission intensities, we used the open-source software package S^4: the Stanford Stratified Structure Solver by Liu and Fan.[65] The rigorous coupled-wave analysis (RCWA) software simulates the propagation of electromagnetic waves through 3D structures with 2D periodicity. Identical to the FDTD simulations, we simulate a TiO_2 nanocylinder, but now in periodic boundary conditions. The real part of the refractive index of TiO_2 is set to $n = 2.32$, according to the measured refractive index at $\lambda = 650$ nm. The extinction coefficient is set to $k \approx 0.02$ ($\mathrm{Im}(\varepsilon) = 0.1$) for the center layer of 30 nm height; the rest of the cylinder is considered lossless.

The emission intensity results are obtained by performing the reciprocal simulation: according to the Helmholtz reciprocity principle, absorption of light at a certain position that is incident from the far-field at a certain angle and polarization is reciprocal with emission of light with the same wavelength from the same position towards the far-field at the same angle and polarization. In contrast to the FDTD simulations, this allowed us to calculate the absorption at all emitter positions in a single simulation with a plane-wave source. The simulation was performed for a wide range of combinations of wavelength, polarization, azimuthal angle, and polar angle. Analogous to the FDTD simulations, the plane-wave source is a "constant current" source. The implication is that the total power in the RCWA simulations scales linearly with the LDOS. In the simulation this yields high-intensity at high-LDOS locations, whereas in the experimental results the impact of high-LDOS locations on the intensity is capped because the emitter is a 'constant power' source (for each absorbed photon, a maximum of one photon can be emitted).

The number of components used in the Fourier series (NG) and the extinction coefficient were tested for convergence—the results are shown in Figure S9, showing convergence for NG = 101 and $k = 0.1$. To find convergence, we calculate the angle-resolved emission with S^4 for several NG values, $\sigma(i)$, and determine the weighted difference between subsequent results, $\Delta\sigma(i)$ and $\Delta\sigma_N(i)$, according to:

$$\Delta\sigma(i) = \sqrt{\frac{\int(\sigma_i - \sigma_{i-1})^2 \mathrm{d}r}{\int(\sigma_i)^2 \mathrm{d}r}}, \Delta\sigma_N(i) = \sqrt{\frac{\int(\sigma_i - \sigma_N)^2 \mathrm{d}r}{\int(\sigma_i)^2 \mathrm{d}r}}$$

where r represents the variable of integration, in this case, the points on the k_x,k_y plane, and N is the most accurate result in the convergence test, in our case NG = 161. The curve for $\Delta\sigma(i)$ indicates the difference between subsequent steps in the convergence test along the variable, while the $\Delta\sigma_N(i)$ curve indicates the difference between a step and the final step.

Electron-Beam Physical Vapor Deposition

The Ti_3O_5 precursor was evaporated by electron-beam heating and precipitated onto the substrate. The base pressure of the chamber was 10^{-7} mbar and was raised to 2.5×10^{-5} mbar by flowing O_2 gas into the chamber. The oxygen flow partially determines the final material stoichiometry. The deposition rate was maintained at 0.2 nm/s.

Spin Coating of CdSe-CdZnS Core–Shell Nanoplatelets

CdSe-CdZnS core-shell nanoplatelets with a graded shell[59] were dispersed in a hexane solution with a concentration of 10 mg NPLs per 1 mL hexane. The solution is spin-coated on top of the first TiO_2 layer at 2000 revolutions per minute (RPM) with 500 RPM/s for 60 s, followed by a curing step on a 60 °C hot plate for 10 min.

Electron-Beam Lithography and Reactive Ion Etching

Ma-N 2403, a negative tone resist, was used as an EBL mask. First, hexamethyldisilazane (HMDS), a resist adhesion promotor, is spin-coated on the sample at 4000 RPM with 1000 RPM/s for 35 s, followed by a curing step on a 150 °C hot plate for 1 min. Then, the undiluted ma-N 2403 solution is spin-coated at 4000 RPM with 1000 RPM/s for 35 s and cured at 90 °C for 4 min. The resulting ma-N mask thickness is 365 nm. When fabricating nanostructures on an insulating substrate like glass, a final layer of Electra 92 is spin-coated to help dissipate the e-beam charge, at 2000 RPM, 400 RPM/s for 40 s. When using a silicon substrate, no additional charge-dissipation layer is necessary.

A Raith Voyager EBL system was used to write the patterns in the mask, operating in 50 keV LC60 mode, write field of 500 μm and dose ~250 μC/cm^2.

The mask was then developed in ma-D 525 resist developer for 50 s, rinsed twice in H_2O for 30 s, and blow-dried under a nitrogen gun.

Finally, the sample was etched in an Oxford Instruments Plasmalab 80 Plus reactive ion etcher for 40 min. Flowing 50 sccm of CHF_3 and 1 sccm O_2 gases, we used a single TiO_2 etch recipe based on ref 62—the NPL layer was also properly etched, without significant over or under etching. The ma-N mask was removed with a 15 min oxygen plasma etch in the same etcher, using a 10 s plasma strike at the start and otherwise 0 W forward power.

Ellipsometry

We used a variable-angle spectroscopic ellipsometer (VASE) from J.A. Woollam Co. to measure the angle- and polarization-dependent reflection spectra of a TiO_2 thin film on a silicon and glass substrate. Using a Cody–Lorentz oscillator in CompleteEASE software, we fitted the complex refractive index of the TiO_2 thin film with a mean squared error (MSE) of 4 (n,k values are plotted in Figure S1). We corroborated the fitted n,k values by measuring reflection and absorption from the TiO_2 thin film, showing excellent agreement with calculated reflection and absorption spectra based on the fitted n,k values (see Figure S2).

Atomic Force Microscopy

AFM images were obtained with a ScanAsyst-AIR probe (Bruker, nominal tip radius 2 nm), operated in PeakForce Tapping mode using a Bruker Dimension Icon AFM.

Spatial Photoluminescence Measurements

For the photoluminescence measurements, a WITec alpha300 RS confocal microscopy setup was used in reflection mode with a 100× magnification, 0.9 NA, air objective. The NPLs were excited with a 532 nm excitation wavelength continuous-wave laser, 1 mW power, 100 ms integration time, and diffraction-limited ~300 nm-diameter spot size. Spectra were collected using the fiber-connected WITec ultra-high throughput spectrometer (UHTS), where the collection by the fiber acts as the confocal pinhole. Given a fiber core of 100 μm in diameter, we calculate a collection spot of 1 μm using FWHM = d_{fiber}/M, with M the magnification of the objective.[68] Given the 0.9 NA, angles up to ~64° are collected.

Angle-Resolved Photoluminescence Measurements

Angle-resolved photoluminescence measurements were conducted in a Fourier microscopy setup, where we illuminated the sample with a 515 nm wavelength pulsed laser, with a repetition rate of 1 MHz and a power of 1.39 mW. The sample is placed facing down in the focus of an inverted microscope immersion oil objective (Plan Apo λ 100× NA = 1.45 oil). We illuminate the sample in epi-mode by focusing the pump beam on the back-focal plane (BFP) of the objective to

https://doi.org/10.1021/acsami.5c21066
ACS Appl. Mater. Interfaces XXXX, XXX, XXX–XXX

achieve a collinear spot of ~40 μm diameter in the sample plane (25 cylinders across for 800 nm pitch; 14 cylinders for 1400 nm pitch). To image angle-resolved photoluminescence from the sample on the detector, we place a lens (Fourier lens) on a flip mount in the focus of the BFP of the objective, via a 1:1 telescope, as is done in ref 69. We remove the pump from the PL signal with a combination of 514 nm dichroic and 550 nm long-pass filters. Given the refractive index of the glass substrate and immersion oil (n = 1.475), we collected angles up to ~79.4°.

■ ASSOCIATED CONTENT

Supporting Information

The Supporting Information is available free of charge at https://pubs.acs.org/doi/10.1021/acsami.5c21066.

Optical data of the TiO_2 layers used in this study (Figures S1 and S2), additional simulated data (Figures S3, S6, S8, and S9), and experimental data (Figures S4, S5, and S7) (PDF)

■ AUTHOR INFORMATION

Corresponding Author

Tom Veeken – *NWO-Institute AMOLF, 1098 XG Amsterdam, The Netherlands*; orcid.org/0000-0002-6235-7836; Email: t.veeken@amolf.nl

Authors

Kyra Orbons – *NWO-Institute AMOLF, 1098 XG Amsterdam, The Netherlands*

Nelson de Gaay Fortman – *NWO-Institute AMOLF, 1098 XG Amsterdam, The Netherlands*; orcid.org/0009-0005-0338-5203

Aurelio A. Rossinelli – *Optical Materials Engineering Laboratory, Department of Mechanical and Process Engineering, ETH Zurich, 8092 Zurich, Switzerland*

David J. Norris – *Optical Materials Engineering Laboratory, Department of Mechanical and Process Engineering, ETH Zurich, 8092 Zurich, Switzerland*; orcid.org/0000-0002-3765-0678

A. Femius Koenderink – *NWO-Institute AMOLF, 1098 XG Amsterdam, The Netherlands*; orcid.org/0000-0003-1617-5748

Albert Polman – *NWO-Institute AMOLF, 1098 XG Amsterdam, The Netherlands*; orcid.org/0000-0002-0685-3886

Complete contact information is available at: https://pubs.acs.org/doi/10.1021/acsami.5c21066

Author Contributions

K.O., T.V., and A.P. conceived the project. K.O. developed the nanocylinder fabrication protocol with embedded emitters and drew the sketches. K.O. and T.V. performed the FDTD simulations, ellipsometry, SEM and PL measurements, and the data analysis. N.d.G.F. and T.V. performed the Fourier measurements. A.F.K. and T.V. performed the RCWA simulations. A.A.R. synthesized the nanoplatelets, under the supervision of D.J.N. T.V. performed the AFM measurements and wrote the original draft. A.F.K. and A.P. supervised the project. All authors provided feedback and contributed to the manuscript.

Notes

There are no conflicts to declare.

■ ACKNOWLEDGMENTS

This work was supported by the Dutch Research Council (NWO). Part of this work was carried out on the Dutch national e-infrastructure with the support of SURF Cooperative.

■ REFERENCES

(1) Enerdata. *Global Energy Statistical Yearbook*. Online Access. https://yearbook.enerdata.net/ (accessed 2025-09-08).

(2) IEA. *Global Energy Review*; **2025**. www.iea.org.

(3) Sinke, W. C. Development of Photovoltaic Technologies for Global Impact. *Renewable Energy* **2019**, *138*, 911–914.

(4) Ehrler, B.; Alarcón-Lladó, E.; Tabernig, S. W.; Veeken, T.; Garnett, E. C.; Polman, A. Photovoltaics Reaching for the Shockley–Queisser Limit. *ACS Energy Lett.* **2020**, *5* (9), 3029–3033.

(5) Garnett, E. C.; Ehrler, B.; Polman, A.; Alarcon-Llado, E. Photonics for Photovoltaics: Advances and Opportunities. *ACS Photonics* **2021**, *8* (1), 61–70.

(6) Almora, O.; Baran, D.; Bazan, G. C.; Berger, C.; Cabrera, C. I.; Catchpole, K. R.; Erten-Ela, S.; Guo, F.; Hauch, J.; Ho-Baillie, A. W. Y.; Jacobsson, T. J.; Janssen, R. A. J.; Kirchartz, T.; Kopidakis, N.; Li, Y.; Loi, M. A.; Lunt, R. R.; Mathew, X.; McGehee, M. D.; Min, J.; Mitzi, D. B.; Nazeeruddin, M. K.; Nelson, J.; Nogueira, A. F.; Paetzold, U. W.; Park, N. G.; Rand, B. P.; Rau, U.; Snaith, H. J.; Unger, E.; Vaillant-Roca, L.; Yip, H. L.; Brabec, C. J. Device Performance of Emerging Photovoltaic Materials (Version 1). *Adv. Energy Mater.* **2021**, *11* (11), No. 2002774.

(7) Blasi, B.; Kroyer, T.; Kuhn, T.; Hohn, O. The MorphoColor Concept for Colored Photovoltaic Modules. *IEEE J. Photovolt.* **2021**, *11* (5), 1305–1311.

(8) Kuhn, T. E.; Erban, C.; Heinrich, M.; Eisenlohr, J.; Ensslen, F.; Neuhaus, D. H. Review of Technological Design Options for Building Integrated Photovoltaics (BIPV). *Energy Build.* **2021**, *231*, No. 110381.

(9) Kryszak, M.; Wang, L. W. The Value of Aesthetics in the BIPV Roof Products Segment: A Multiperspective Study under European Market Conditions. *Energy Sources, Part A* **2020**, *46* (1), 14635–14656.

(10) Bergren, M. R.; Makarov, N. S.; Ramasamy, K.; Jackson, A.; Guglielmetti, R.; McDaniel, H. High-Performance $CuInS_2$ Quantum Dot Laminated Glass Luminescent Solar Concentrators for Windows. *ACS Energy Lett.* **2018**, *3* (3), 520–525.

(11) Meinardi, F.; Bruni, F.; Brovelli, S. Luminescent Solar Concentrators for Building-Integrated Photovoltaics. *Nat. Rev. Mater.* **2017**, *2*, No. 17072.

(12) Traverse, C. J.; Pandey, R.; Barr, M. C.; Lunt, R. R. Emergence of Highly Transparent Photovoltaics for Distributed Applications. *Nat. Energy* **2017**, *2* (11), 849–860.

(13) Husain, A. A. F.; Hasan, W. Z. W.; Shafie, S.; Hamidon, M. N.; Pandey, S. S. A Review of Transparent Solar Photovoltaic Technologies. *Renewable Sustainable Energy Rev.* **2018**, *94*, 779–791.

(14) de Bruin, T. A.; van Sark, W. G. J. H. M. Shining Lights on Limits: Optimizing Luminescent Solar Concentrators for Solar Windows. *Adv. Photonics Res.* **2025**, *6* (1), No. 2400068.

(15) Lamnatou, C.; Chemisana, D. Solar Radiation Manipulations and Their Role in Greenhouse Claddings: Fluorescent Solar Concentrators, Photoselective and Other Materials. *Renewable Sustainable Energy Rev.* **2013**, *27*, 175–190.

(16) Loik, M. E.; Carter, S. A.; Alers, G.; Wade, C. E.; Shugar, D.; Corrado, C.; Jokerst, D.; Kitayama, C. Wavelength-Selective Solar Photovoltaic Systems: Powering Greenhouses for Plant Growth at the Food-Energy-Water Nexus. *Earths Future* **2017**, *5* (10), 1044–1053.

(17) Reinders, A.; Kishore, R.; Slooff, L.; Eggink, W. Luminescent Solar Concentrator Photovoltaic Designs. *Jpn. J. Appl. Phys.* **2018**, *57* (8S3), No. 08RD10.

(18) Renny, A.; Yang, C.; Anthony, R.; Lunt, R. R. Luminescent Solar Concentrator Paintings: Connecting Art and Energy. *J. Chem. Educ.* **2018**, *95* (7), 1161–1166.

(19) Castelletto, S.; Boretti, A. Luminescence Solar Concentrators: A Technology Update. *Nano Energy* **2023**, *109*, No. 108269.
(20) Yang, C.; Liu, D.; Bates, M.; Barr, M. C.; Lunt, R. R. How to Accurately Report Transparent Solar Cells. *Joule* **2019**, *3* (8), 1803–1809.
(21) Debije, M. G.; Verbunt, P. P. C. Thirty Years of Luminescent Solar Concentrator Research: Solar Energy for the Built Environment. *Adv. Energy Mater.* **2012**, *2* (1), 12–35.
(22) Rajkumar, V. A.; Weijers, C.; Debije, M. G. Distribution of Absorbed Heat in Luminescent Solar Concentrator Lightguides and Effect on Temperatures of Mounted Photovoltaic Cells. *Renewable Energy* **2015**, *80*, 308–315.
(23) Baikie, T. K.; Daiber, B.; Kensington, E.; Xiao, J.; Greenham, N. C.; Ehrler, B.; Rao, A. Revealing the Potential of Luminescent Solar Concentrators in Real-World Environments. *Joule* **2024**, *8* (3), 799–816.
(24) Debije, M. G.; Rajkumar, V. A. Direct versus Indirect Illumination of a Prototype Luminescent Solar Concentrator. *Solar Energy* **2015**, *122*, 334–340.
(25) Einhaus, L. M.; Heres, G. C.; Westerhof, J.; Pal, S.; Kumar, A.; Zheng, J.-Y.; Saive, R. Free-Space Diffused Light Collimation and Concentration. *ACS Photonics* **2023**, *10* (2), 508–517.
(26) Hanifi, D. A.; Bronstein, N. D.; Koscher, B. A.; Nett, Z.; Swabeck, J. K.; Takano, K.; Schwartzberg, A. M.; Maserati, L.; Vandewal, K.; van de Burgt, Y.; Salleo, A.; Alivisatos, A. P. Redefining Near-Unity Luminescence in Quantum Dots with Photothermal Threshold Quantum Yield. *Science* **2019**, *363* (6432), 1199–1202.
(27) Wu, K.; Li, H.; Klimov, V. I. Tandem Luminescent Solar Concentrators Based on Engineered Quantum Dots. *Nat. Photonics* **2018**, *12* (2), 105–110.
(28) Needell, D. R.; Ilic, O.; Bukowsky, C. R.; Nett, Z.; Xu, L.; He, J.; Bauser, H.; Lee, B. G.; Geisz, J. F.; Nuzzo, R. G.; Alivisatos, A. P.; Atwater, H. A. Design Criteria for Micro-Optical Tandem Luminescent Solar Concentrators. *IEEE J. Photovolt.* **2018**, *8* (6), 1560–1567.
(29) Needell, D. R.; Bukowsky, C. R.; Darbe, S.; Bauser, H.; Ilic, O.; Atwater, H. A. Spectrally Matched Quantum Dot Photoluminescence in GaAs-Si Tandem Luminescent Solar Concentrators. *IEEE J. Photovolt.* **2019**, *9* (2), 1–5.
(30) Eisler, C. N.; Parsons, L. E.; Nett, Z.; Love, C.; Schwartzberg, A. M.; Alivisatos, A. P. Photonic Luminescent Solar Concentrator Design for High Efficiency, Low Cost Multijunction Photovoltaics. *Front. Photonics* **2022**, *3*, No. 932913.
(31) van der Burgt, J. S.; Needell, D. R.; Veeken, T.; Polman, A.; Garnett, E. C.; Atwater, H. A. Unlocking Higher Power Efficiencies in Luminescent Solar Concentrators through Anisotropic Luminophore Emission. *ACS Appl. Mater. Interfaces* **2021**, *13* (34), 40742–40753.
(32) Yablonovitch, E. Thermodynamics of the Fluorescent Planar Concentrator. *J. Opt. Soc. Am.* **1980**, *70* (11), No. 1362.
(33) Smestad, G.; Ries, H.; Winston, R.; Yablonovitch, E. The Thermodynamic Limits of Light Concentrators. *Solar Energy Mater.* **1990**, *21* (2–3), 99–111.
(34) Meinardi, F.; Ehrenberg, S.; Dhamo, L.; Carulli, F.; Mauri, M.; Bruni, F.; Simonutti, R.; Kortshagen, U.; Brovelli, S. Highly Efficient Luminescent Solar Concentrators Based on Earth-Abundant Indirect-Bandgap Silicon Quantum Dots. *Nat. Photonics* **2017**, *11* (3), 177–185.
(35) Knowles, K. E.; Kilburn, T. B.; Alzate, D. G.; McDowall, S.; Gamelin, D. R. Bright $CuInS_2$/CdS Nanocrystal Phosphors for High-Gain Full-Spectrum Luminescent Solar Concentrators. *Chem. Commun.* **2015**, *51* (44), 9129–9132.
(36) Roncali, J. Luminescent Solar Collectors: Quo Vadis? *Adv. Energy Mater.* **2020**, *10* (36), No. 2001907.
(37) Slooff, L. H.; Bende, E. E.; Burgers, A. R.; Budel, T.; Pravettoni, M.; Kenny, R. P.; Dunlop, E. D.; Büchtemann, A. A Luminescent Solar Concentrator with 7.1% Power Conversion Efficiency. *Phys. Status Solidi RRL* **2008**, *2* (6), 257–259.
(38) Bronstein, N. D.; Yao, Y.; Xu, L.; O'Brien, E.; Powers, A. S.; Ferry, V. E.; Alivisatos, A. P.; Nuzzo, R. G. Quantum Dot Luminescent Concentrator Cavity Exhibiting 30-Fold Concentration. *ACS Photonics* **2015**, *2* (11), 1576–1583.
(39) Xu, L.; Yao, Y.; Bronstein, N. D.; Li, L.; Alivisatos, A. P.; Nuzzo, R. G. Enhanced Photon Collection in Luminescent Solar Concentrators with Distributed Bragg Reflectors. *ACS Photonics* **2016**, *3* (2), 278–285.
(40) de Boer, D. K. G.; Broer, D. J.; Debije, M. G.; Keur, W.; Meijerink, A.; Ronda, C. R.; Verbunt, P. P. C. Progress in Phosphors and Filters for Luminescent Solar Concentrators. *Opt. Express* **2012**, *20* (S3), No. A395.
(41) Heres, G. C.; Einhaus, L. M.; Saive, R. Analytical Model for the Performance of a Free-Space Luminescent Solar Concentrator. *Conf. Rec. IEEE Photovoltaic Spec. Conf.* **2021**, 1027–1029.
(42) Bronstein, N. D.; Li, L.; Xu, L.; Yao, Y.; Ferry, V. E.; Alivisatos, A. P.; Nuzzo, R. G. Luminescent Solar Concentration with Semiconductor Nanorods and Transfer-Printed Micro-Silicon Solar Cells. *ACS Nano* **2014**, *8* (1), 44–53.
(43) Bradshaw, L. R.; Knowles, K. E.; McDowall, S.; Gamelin, D. R. Nanocrystals for Luminescent Solar Concentrators. *Nano Lett.* **2015**, *15* (2), 1315–1323.
(44) Fisher, M.; Farrell, D.; Zanella, M.; Lupi, A.; Stavrinou, P. N.; Chatten, A. J. Utilizing Vertically Aligned CdSe/CdS Nanorods within a Luminescent Solar Concentrator. *Appl. Phys. Lett.* **2015**, *106* (4), 3–6.
(45) Bauser, H. C.; Bukowsky, C. R.; Phelan, M.; Weigand, W.; Needell, D. R.; Holman, Z. C.; Atwater, H. A. Photonic Crystal Waveguides for 90% Light Trapping Efficiency in Luminescent Solar Concentrators. *ACS Photonics* **2020**, *7* (8), 2122–2131.
(46) Vaskin, A.; Kolkowski, R.; Koenderink, A. F.; Staude, I. Light-Emitting Metasurfaces. *Nanophotonics* **2019**, *8* (7), 1151–1198.
(47) Rybin, M. V.; Kivshar, Y. Metaphotonics with Subwavelength Dielectric Resonators. *npj Nanophotonics* **2024**, *1* (1), No. 43.
(48) Babicheva, V. E.; Evlyukhin, A. B. Mie-Resonant Metaphotonics. *Adv. Opt. Photonics* **2024**, *16* (3), No. 539.
(49) van der Burgt, J. S.; Garnett, E. C. Nanophotonic Emission Control for Improved Photovoltaic Efficiency. *ACS Photonics* **2020**, *7* (7), 1589–1602.
(50) Mertens, H.; Biteen, J. S.; Atwater, H. A.; Polman, A. Polarization-Selective Plasmon-Enhanced Silicon Quantum-Dot Luminescence. *Nano Lett.* **2006**, *6* (11), 2622–2625.
(51) Curto, A. G.; Volpe, G.; Taminiau, T. H.; Kreuzer, M. P.; Quidant, R.; van Hulst, N. F. Unidirectional Emission of a Quantum Dot Coupled to a Nanoantenna. *Science* **2010**, *329* (5994), 930–933.
(52) Mertens, H.; Polman, A. Plasmon-Enhanced Erbium Luminescence. *Appl. Phys. Lett.* **2006**, *89* (21), No. 211107.
(53) Rodriguez, S. R. K.; Arango, F. B.; Steinbusch, T. P.; Verschuuren, M. A.; Koenderink, A. F.; Rivas, J. G. Breaking the Symmetry of Forward-Backward Light Emission with Localized and Collective Magnetoelectric Resonances in Arrays of Pyramid-Shaped Aluminum Nanoparticles. *Phys. Rev. Lett.* **2014**, *113* (24), No. 247401.
(54) Staude, I.; Pertsch, T.; Kivshar, Y. S. All-Dielectric Resonant Meta-Optics Lightens Up. *ACS Photonics* **2019**, *6* (4), 802–814.
(55) Watkins, N. E.; Guan, J.; Diroll, B. T.; Williams, K. R.; Schaller, R. D.; Odom, T. W. Surface Normal Lasing from CdSe Nanoplatelets Coupled to Aluminum Plasmonic Nanoparticle Lattices. *J. Phys. Chem. C* **2021**, *125* (36), 19874–19879.
(56) Aellen, M.; Rossinelli, A. A.; Keitel, R. C.; Brechbühler, R.; Antolinez, F. V.; Rodrigo, S. G.; Cui, J.; Norris, D. J. Role of Gain in Fabry–Pérot Surface Plasmon Polariton Lasers. *ACS Photonics* **2022**, *9* (2), 630–640.
(57) Wu, M.; Ding, L.; Sabatini, R. P.; Sagar, L. K.; Bappi, G.; Paniagua-Domínguez, R.; Sargent, E. H.; Kuznetsov, A. I. Bound State in the Continuum in Nanoantenna-Coupled Slab Waveguide Enables Low-Threshold Quantum-Dot Lasing. *Nano Lett.* **2021**, *21* (22), 9754–9760.
(58) Veeken, T.; Daiber, B.; Agrawal, H.; Aarts, M.; Alarcón-Lladó, E.; Garnett, E. C.; Ehrler, B.; van de Groep, J.; Polman, A. Directional Quantum Dot Emission by Soft-Stamping on Silicon Mie Resonators. *Nanoscale Adv.* **2022**, *4* (4), 1088–1097.
(59) Rossinelli, A. A.; Rojo, H.; Mule, A. S.; Aellen, M.; Cocina, A.; De Leo, E.; Schäublin, R.; Norris, D. J. Compositional Grading for Efficient and Narrowband Emission in CdSe-Based Core/Shell Nanoplatelets. *Chem. Mater.* **2019**, *31* (22), 9567–9578.

https://doi.org/10.1021/acsami.5c21066
ACS Appl. Mater. Interfaces XXXX, XXX, XXX–XXX

(60) Mie, G. Beiträge Zur Optik Trüber Medien, Speziell Kolloidaler Metallösungen. *Ann. Phys.* **1908**, *330* (3), 377–445.
(61) van de Groep, J.; Polman, A. Designing Dielectric Resonators on Substrates: Combining Magnetic and Electric Resonances. *Opt. Express* **2013**, *21* (22), No. 26285.
(62) Ha, S.; Janissen, R.; Ussembayev, Y. Y.; Van Oene, M. M.; Solano, B.; Dekker, N. H. Tunable Top-down Fabrication and Functional Surface Coating of Single-Crystal Titanium Dioxide Nanostructures and Nanoparticles. *Nanoscale* **2016**, *8* (20), 10739–10748.
(63) Van De Groep, J.; Spinelli, P.; Polman, A. Single-Step Soft-Imprinted Large-Area Nanopatterned Antireflection Coating. *Nano Lett.* **2015**, *15* (6), 4223–4228.
(64) Vaskin, A.; Liu, S.; Addamane, S.; Vabishchevich, P. P.; Yang, Y.; Balarishnan, G.; Sinclair, M. B.; Pertsch, T.; Brener, I.; Staude, I. Manipulation of Quantum Dot Emission with Semiconductor Metasurfaces Exhibiting Magnetic Quadrupole Resonances. *Opt. Express* **2021**, *29* (4), 5567.
(65) Liu, V.; Fan, S. S4: A Free Electromagnetic Solver for Layered Periodic Structures. *Comput. Phys. Commun.* **2012**, *183* (10), 2233–2244.
(66) ANSYS Lumerical. *FDTD Solutions 2022 R1.2*, **2022**. https://www.ansys.com/products/optics/fdtd (accessed 2025-05-04).
(67) Novotny, L.; Hecht, B. *Principles of Nano-Optics*; Cambridge University Press: Cambridge, **2012**, *9781107005*.
(68) Brakenhoff, G. J.; Visscher, K.; van der Voort, H. T. M. Size and Shape of The Confocal Spot: Control and Relation to 3D Imaging and Image Processing. In *Handbook of Biological Confocal Microscopy*; Springer US: Boston, MA, **1990**, 87–91.
(69) Sersic, I.; Tuambilangana, C.; Femius Koenderink, A. Fourier Microscopy of Single Plasmonic Scatterers. *New J. Phys.* **2011**, *13* (8), No. 083019.

https://doi.org/10.1021/acsami.5c21066
ACS Appl. Mater. Interfaces XXXX, XXX, XXX–XXX